Microchimica Acta (2023) 190:43
https://doi.org/10.1007/s00604-022-05615-9

ORIGINAL PAPER

Ion-selective electrodes based on laser-induced graphene as an alternative method for nitrite monitoring

Raquel R. A. Soares[1] · Robert G. Hjort[1] · Cícero C. Pola[1] · Dapeng Jing[2] · Victor S. Cecon[3] · Jonathan C. Claussen[1] · Carmen L. Gomes[1]

Received: 6 October 2022 / Accepted: 5 December 2022

Abstract

Nitrite is an important food additive for cured meats; however, high nitrite levels pose adverse health effects to humans. Hence, monitoring nitrite concentration is critical to comply with limits imposed by regulatory agencies. Laser-induced graphene (LIG) has proven to be a scalable manufacturing alternative to produce high-performance electrochemical transducers for sensors. Herein, we expand upon initial LIG studies by fabricating hydrophilic and hydrophobic LIG that are subsequently converted into ion-selective sensors to monitor nitrite in food samples with comparable performance to the standard photometric method (Griess method). The hydrophobic LIG resulted in an ion-selective electrode with improved potential stability due partly to a decrease in the water layer between the electrode and the nitrite poly(vinyl) chloride-based ion-selective membrane. These resultant nitrite ion-selective sensors displayed Nernstian response behavior with a sensitivity of 59.5 mV dec^{-1}, a detection limit of 0.3 ± 0.1 mg L^{-1} (mean ± standard deviation), and a broad linear sensing range from 10^{-5} to 10^{-1} M, which was significantly larger than currently published nitrite methods. Nitrite levels were determined directly in food extract samples of sausage, ham, and bacon for 5 min. These sensor metrics are significant as regulatory agencies limit nitrite levels up to 200 mg L^{-1} in finished products to reduce the potential formation of nitrosamine (carcinogenic compound). These results demonstrate the versatility of LIG as a platform for ion-selective-LIG sensors and simple, efficient, and scalable electrochemical sensing in general while demonstrating a promising alternative to monitor nitrite levels in food products ensuring regulatory compliance.

Keywords Graphene · Solid-contact ion selective electrodes · Potentiometry · Electrochemical Sensors · Food safety · Food additives

Introduction

Nitrite salts are one of the most important additives applied in the curing process of meat products [1–3]. These salts not only improve the color and flavor of cured meats but also play a major role as inhibitors of microbial growth, in particular, *Clostridium botulinum* [4–7]. Nonetheless, the use of nitrite salts as a preservative and curing agent has raised concerns about human health as nitrite reacts with hemoglobin to form methemoglobin, which reduces the capacity of blood to carry oxygen, in addition to reacting with secondary amines and amides to form the potentially carcinogenic compounds, N-nitrosamines [8, 9]. Thus, limitations to nitrite levels in food products and drinking water have been implemented, with regulations varying from country to country, as studies began to show that low contents of nitrite salts do not promote relevant levels of N-nitrosamines formation [10–12]. For instance, in the USA, sodium nitrite has a maximum limit that varies with cured meat type from 120 to 200 ppm, according to the USDA, and as low as 1 ppm in drinking water, according to the EPA [13, 14]. Given the importance of quantifying nitrite, there is a need for reliable and rapid methods to monitor its levels in food products; ideally, methods that do not require complex or costly manufacturing processes and are easy to use, with minimal sample preparation.

✉ Carmen L. Gomes
carmen@iastate.edu

[1] Department of Mechanical Engineering, Iowa State University, Ames, IA 50011, USA

[2] Materials Analysis and Research Laboratory, Iowa State University, Ames, IA 50011, USA

[3] Department of Food Science and Human Nutrition, Iowa State University, Ames, IA 50011, USA

Published online: 03 January 2023

The range of analytical methods for nitrite monitoring has been comprehensively reviewed by other groups [15–17] with electrochemical sensors providing rapid, sensitive, and portable alternatives to other analytical methodologies, including spectrophotometric [18], chromatographic [19–21], capillary electrophoresis [22], spectrofluorimetric [23–25], colorimetric [26–29], and electrochemiluminescent [30] techniques. The current standard Griess method (AOAC official method 973.31), a colorimetric method, requires trained personnel and is time-limited since the solutions expire 8 h after preparation, and time-consuming with sample preparation and dilutions required to accommodate its linear range [31].

Carbon nanomaterials such as graphene are being explored in various electrochemical applications due to their large surface area, high electrical conductivity, mechanical resistance, and thermal conductivity [32–34]. In particular, 3D-carbon nanomaterials, such as graphene sponge, carbon nanofibers, micro/nanostructure printed graphene, and laser-induced graphene, build upon these material properties by providing an electrode with much higher surface area for increased analyte-to-electrode interaction and biorecognition agent loading, and consequently higher biosensor sensitivity [35]. There are many methods for fabrication of 3D-graphene structures, including electrochemical deposition [36], freeze-drying [37], and hydrothermal synthesis [38]; however, issues with integrating as-fabricated 3D graphene into electrochemical sensors reduce their high-throughput and scalable fabrication. To simplify the 3D-graphene sensor fabrication, various printing techniques, including inkjet [39, 40], screen [41], and 3D printing [42, 43], have been explored. However, post-print annealing techniques such as high-temperature [44], photonic [45], and rapid-pulse laser annealing [39] are required to improve electrical conductivity (similar to printed metals, i.e., < 1 k Ω) and 3D nano/micro structuring.

Another promising approach for 3D-graphene-based sensors is to use a laser treatment that combines direct-write printing and post-print annealing to fabricate highly porous, 3D-graphene-based structures. In 1991, Schumann et al. demonstrated that a UV laser treatment to polymers such as polyimide and polybenzimidazole converted them into conductive materials [46]. The Tour group at Rice University in 2014 used a CO_2 laser to convert polyimide [47] and other materials [48] into a 3D porous graphene structure, known as laser-induced graphene (LIG). Such LIG material has disordered graphitic structures that expose edge sites, promoting efficient electron transfer of electroactive species [49, 50]. Additionally, LIG surface chemical and physical properties such as porosity, thickness, electrical conductivity, and surface hydrophobicity can be tuned [51]. Recent studies in LIG formation and surface properties, including ours [52, 53], have demonstrated that controlling laser power, focus, and the number of lasing steps can create LIG with super-hydrophilic or super-hydrophobic surfaces, even in the open ambient in some cases, improving conductivity and electrochemical performance for sensing applications [51, 54–56]. Understanding these properties allows for the reliable fabrication of scalable electrodes.

Potentiometric ion-selective electrodes have been applied for sensitive and selective ion monitoring [57, 58] in many applications that include in-field water environment analysis (heavy metals, perchlorate, calcium, and iodide) [59–64] to in vivo biomedical applications (potassium, calcium, nitric oxide, lithium) [65–69]. Traditional liquid-junction ISEs have an inner liquid (electrolyte) that requires maintenance due to liquid leaching. In contrast, solid-contact ion-selective electrodes (SC-ISEs) remove this inner liquid allowing the ion-selective membrane to make direct contact with the transducing layer. To replace the liquid-junction, SC-ISEs must exhibit minimal potential drift between the transducer and ion-selective membrane [70, 71]. LIG-based electrodes have the potential to fulfill these requirements and to be a promising solid-contact transducer for the fabrication of SC-ISEs, as explored in recent studies regarding fertilizer monitoring in soil (NO_3^- and NH_4^+) [72], evaluating human hydration levels and pH in urine (K^+ and NH_4^+) [73, 74], as well as human sweat monitoring [75, 76], and surface water quality monitoring (NO_3^-) [52]. Despite their advantages, LIG-ISE for nitrite sensing has not been explored. Most electrochemical detection of nitrite is based on electrochemical oxidation or reduction. However, problems with electrode-passivation and fouling effects can occur, reducing the sensitivity of the method, which has been circumvented with the use of power ultrasound to clean the electrode [77], nevertheless, affecting portability and in-field applications. Additionally, most electrochemical sensors for nitrite require multiple and laborious steps to fabricate the electrodes, with detection ranges that are not within the regulated levels for food analysis (upper limit of 200 ppm) [78]. The detection ranges are often in the nanomolar range, except for a few cases, requiring several dilutions and sample preparation steps, and are mostly limited to proof-of-concept demonstration in water samples [78].

In the present work, we successfully developed a nitrite-selective potentiometric sensor based on LIG to measure nitrite levels in cured meats. For this purpose, we systematically fabricated hydrophilic and hydrophobic LIG-electrodes using a CO_2 laser and evaluated the electrochemical and material properties. To characterize the material changes, we evaluated the resulting LIG surfaces for their morphology (SEM), surface composition and chemical structure (XPS and Raman), and static contact angle, providing a correlation between the LIG platform and the resultant electrochemical properties. We showed that the double-lasing process reduces the surface oxygen

content, increases the contact angle, and the sp^2 carbon content, exhibiting a better performance as a material for ion-sensing applications. The resulting LIG-ISE sensor is capable of monitoring nitrite in cured meats, with results comparable to the standard method (Griess method) and within the range imposed by the USDA regulations [13].

Experimental section

Materials

Nitrite ionophore VI, tetrahydrofuran (THF), high-molecular-weight polyvinyl(chloride) (PVC), 2-nitrophenyl octyl ether (2-NPOE), sodium nitrite, sodium nitrate, potassium hexacyanoferrate (II) trihydrate, potassium ferricyanide, and the Griess reagent kit for nitrite determination (G-7921) were purchased from Millipore Sigma (Saint Louis, MO, USA). Commercial polyimide (PI) was purchased from McMaster-Carr (Elmhurst, IL, USA), and silver-chloride epoxy ink (Cl-1001) from Engineering Materials Systems (Delaware, OH, USA). Sodium chloride, potassium chloride, potassium sulfate, and ELISA microplates were obtained from Thermo Fisher Scientific (Waltham, MA, USA). Sausage, ham, and bacon were purchased at a local grocery store. All chemicals were analytical grade, and solutions were prepared using deionized (DI) water with a resistivity of approximately 18.2 MΩ cm.

Fabrication of LIG-electrodes

Hydrophilic and hydrophobic electrodes were fabricated using a 75-W M2 Epilog CO_2 laser, wavelength 10.6 mm, (Epilog Laser, CO, USA), and a polyimide film, thickness ~ 0.127 mm, under ambient conditions, as previously reported [52]. Hydrophilic LIG-electrodes (1X-LIG) were fabricated using a single-lasing process. Meanwhile, hydrophobic LIG-electrodes (2X-LIG) were fabricated using a successive double-lasing process. The electrodes presented a circular working area (5 mm in diameter), shown in Fig. 1, and a squared contact pad (9 mm^2) at the other end protected with conductive silver paste. The portion between the two

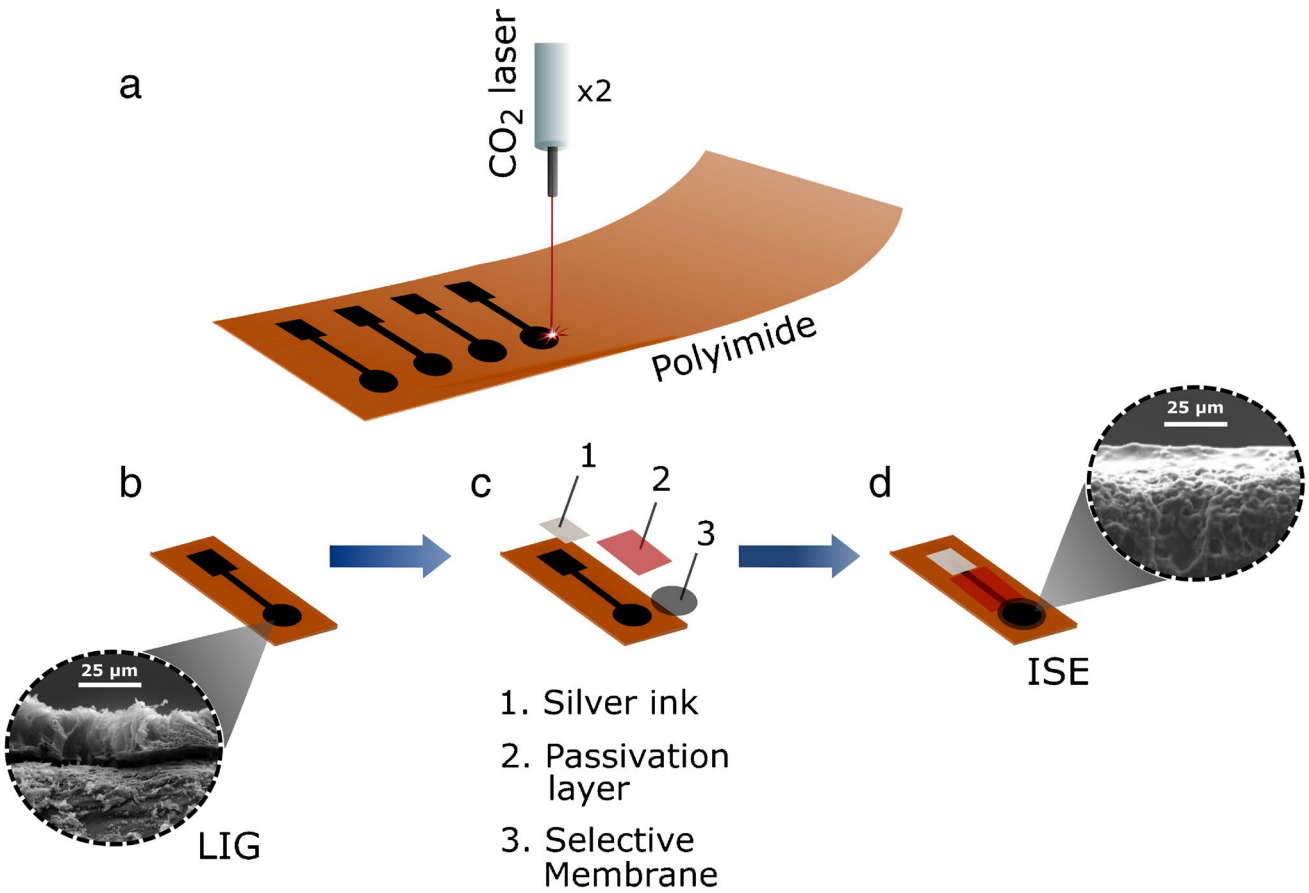

Fig. 1 Fabrication steps for a LIG-based ion-selective electrode (ISE). **a** Laser-induction process onto a polyimide film. **b** Cross-sectional SEM image of the working electrode area. **c** Application of the three main components that make up the ISE. **d** Cross-sectional SEM image of the working area covered with the ion-selective membrane

ends was isolated by applying a passivation layer of fast-drying nitrocellulose-based lacquer.

The nitrite-selective membrane was prepared by dissolving 6.4 wt.% nitrite ionophore VI, the main compound of the membrane used to promote the ionic exchange, 24.7 wt.% PVC, the polymeric substrate, 68.9 wt.% 2-NPOE, the plasticizer that helps solubilize the ionophore and is inert to ion exchange, in 1 mL of THF, the solvent that allows the mixing of the other components, which will be completely evaporated. The mixture of chemicals was stirred using a vortex until the compounds were completely dissolved; then, 10 µL of the fresh membrane was drop-casted onto the working area of the LIG-electrodes. After overnight drying, the ion-selective electrodes (ISEs) were conditioned in 1 mM $NaNO_2$ for 24 h before being tested, as a crucial step for the selective membrane to reach an optimum target-ion concentration and ensure that the measured potential would be stable [79, 80].

Surface characterization

Bare electrodes were characterized considering the two lasing processes, which provided hydrophilic and hydrophobic graphene-based surfaces. Sheet resistances of both electrodes were measured with a Hall measurement system (MMR H5000, MMR Technologies, San Jose, CA, USA) using the Van der Pauw method with a 1 × 1 cm sample and electrical contact at the four corners. The static contact angle measurements were performed using a ramé-hart model 90 goniometer (ramé-hart instrument co., Succasunna, NJ, USA), applying a 3-µL droplet of pure water onto the surface of the electrodes. Angle measurements were performed using the software DROPimage Pro (ramé-hart instrument co., Succasunna, NJ, USA).

Raman spectra were obtained using a DXR Raman Microscope (Thermo Fisher, Waltham, MA, USA), with acquisitions of 32 scans under an exposure time of 7.5 s and a 2 cm^{-1} resolution. A 780-nm laser operating at 20 mW with a 10 × objective was used. The results were analyzed with OMNIC™ 9.7 software (Thermo Fisher, Waltham, MA, USA).

The surface chemistry of the bare LIG-electrodes was analyzed through X-ray photoelectron spectroscopy (XPS), performed with a Kratos Amicus/ESCA 3400 (Kratos Analytical, Manchester, UK). Unmonochromated Mg K_α X-rays were irradiated on the samples with 240 W, and the energy of photoelectrons vertically emitted were analyzed using a DuPont type analyzer. The pass energy was set at 150 eV, and the raw data were processed using CasaXPS (Casa Software Ltd., Teignmouth, UK).

Top-view and cross-sectioned images from scanning electron microscopy (SEM) were obtained using a FEI Quanta 250 field emission microscope (FEI Technologies, Hillsboro, OR, USA) at 150 ×, 500 ×, and 1500 × magnification, and at an accelerating voltage of 10 kV. The material samples were coated with 2-nm iridium to increase the conductivity.

Electrochemical characterization and sensing

Cyclic voltammetry (CV) and constant current chronopotentiometry (CP) measurements were performed using a CH Instruments electrochemical analyzer (model CHI7018E, CH Instruments Inc., Austin, TX, USA). All experiments were conducted with the developed electrodes as the working electrode and an external Ag/AgCl electrode with a 1 M KCl liquid junction as the reference electrode. CP and CV analyses used a three-electrode set-up with a platinum wire electrode as the counter electrode and an Ag/AgCl electrode as the reference electrode. Open-circuit potentiometry (OCP) was used to calibrate the sensors, conduct the selectivity and water layer tests, and nitrite sensing. All OCP measurements were obtained using a PalmSens4 potentiostat (PalmSens, Netherlands) equipped with a MUX8-R2 multiplexer.

Cyclic voltammetric measurements for 1X-LIG and 2X-LIG were performed in 5 mM ferro/ferricyanide redox probe, prepared in 0.1 M KCl as the electrolyte, with potential sweep ranging from − 0.4 to 1.0 V, and scan rates of 10, 25, 50, 75, 100, and 150 mV s^{-1}. These voltammograms were used to estimate the electroactive surface area (ESA) of the electrodes (see Supplementary information for details, Eq. S1).

Analysis based on chronopotentiometry and water layer test were used to measure the potential stability of the ISEs. For the CP measurements, after a previous conditioning step in 0.1 M $NaNO_2$ for 24 h, a current of ± 1 nA was applied for 60 s each (120 s total), and the potential was recorded with electrodes immersed in 0.1 M $NaNO_2$.

The water layer test was carried out by measuring the OCP of the ISEs made from both 1X-LIG and 2X-LIG electrodes over 24 h. The electrodes were first exposed to a 1 mM solution of target ion ($NaNO_2$) for 4 h, followed by 1 mM solution of an interfering ion (KCl) for another 4 h, and finally returned to the initial target ion solution for a 16-h incubation step, with rinsing steps between transfers [72].

The developed ISEs based on 1X-LIG and 2X-LIG substrate were calibrated from 10^{-7} to 10^{-1} M $NaNO_2$ with additions at each 0.5 log. Calibrations were performed in DI water under agitation at 300 rpm. Ionic activity coefficients were calculated using the extended Debye-Hückel equation (Eq. S3 in Supplementary information). Selectivity coefficients were obtained by the fixed-interference method [81] for three specimens of ions common in cured food (Cl^-, NO_3^-, and $H_2PO_4^-$). For this analysis, similar to the calibrations described above, a large range of $NaNO_2$

concentrations was added into a constant concentration of 1 mM of each interfering ion. Then, the selectivity coefficients were calculated using Eq. S5 (see Supplementary information). The "response time" was the time required to reach 95% of the steady-state signal (t95) after each target ion addition. The sensitivity was obtained as the mean slope of the linear portion of the calibration curve, and the limit of detection (LOD) was calculated using the 3 σ method [82].

For sensing purposes, the OCP method was used to measure the electrical potential difference between the reference electrode and the working electrode, also called electromotive force (emf). By substituting the measured emf value into the respective linear equation obtained from the calibration curve in DI water, it is possible to estimate the concentration of target ions, using ionic activity equation (see Supplemental information Eq. S2-S3). This ionic activity relates to the actual concentration of the target ion in the solution (see Supplemental, Fig. S4e). The standard colorimetric method for nitrite detection using the Griess reagent kit [83] was performed to validate the method proposed in this work. The Griess method is based on quantitative diazotization of nitrite with sulfanilic acid, and the formed salt reacts with N-(1-naphthyl)ethylenediamine (NED), forming an azo dye that can be quantitatively estimated by spectrophotometry with readings at 548 nm, according to the information stated in the kit manual. A linear calibration curve is obtained by measuring the absorbance of different nitrite concentrations (Fig. 4b).

Preparation of food samples

Three different types of cured meat were tested to validate the developed sensors (Fig. S1). For extracting nitrite from the food samples, 30 g of each food product were sliced and crushed using a mortar and pestle to increase the surface area and facilitate nitrite extraction, then stirred in 300 mL DI water at 70 °C for 10 min, following previous established protocol [84]. The extracted solution was filtered to remove large food fragments and then centrifuged at 3260 *g*-force for 15 min, using a Thermo Scientific Sorvall ST-8R centrifuge (Waltham, MA, USA). Finally, the supernatant was filtered with a 0.45-µm sterile syringe filter made of surfactant-free cellulose acetate (Corning Incorporated, Germany).

Data analysis

The data analysis for calibration curves, including regression analysis, calculations of sensitivity, and LOD was performed using MATLAB (R2020a, The MathWorks Inc., Natick, MA, USA). The *t* test with a significance level of 0.05 was performed to compare the two methods for nitrite determination and to compare the two different surfaces of electrodes (hydrophilic and hydrophobic LIG) using JMP Pro v.15 statistical software (SAS Institute, Cary, NC, USA). All figures were plotted in SigmaPlot 14 (Systat Software Inc., San Jose, CA).

Results and discussion

Surface characterization of bare electrodes

The LIG-electrodes were patterned in a dipstick design presenting a 5-mm diameter circle with a 15-mm long stem and a 9-mm^2 contact pad (Fig. 2a). The circular part of the electrodes was used as the working area (with 19.63 mm^2) for the subsequent deposition of the ion-selective membrane. The surface morphology of the electrodes was evaluated using SEM (Fig. 2d–f). Overall, the lasing process generated a highly porous 3-dimensional structure resulting in a high surface area. More specifically, 1X-LIG presented vertically aligned fibers [85] of various heights (Fig. 2d and S2a–b). Such features were flattened by the second lasing process, which made the surface more homogeneous and exposed the rastering traces created by the lasing process. The influence of the single- and double-lasing process on the morphology of LIG has been previously reported by Chen et al. (2021) when tunning the lasing process for the fabrication of hydrophobic LIG [53]. Hjort et al. (2022) observed similar changes in surface morphology after the second lasing process when developing ion selective electrodes for nitrate sensing [52]. Furthermore, cross-sectional images of the SC-ISEs confirm that the ion-selective membrane applied to 1X-LIG generates thinner films due to the membrane flowing over the electrode stem, which considerably impacts the water layer test, further discussed below (Fig. S5b–e). Static water contact angle measurements demonstrated the difference in surface wettability generated by the different lasing processes. The second lasing process significantly increased the hydrophobicity of the LIG-electrodes changing it from $30.2° \pm 1.3°$ (first lasing) to $133.4° \pm 0.4°$. This near-superhydrophobic surface presents a strong water repulsion characteristic that is relevant for the development of ion-selective electrodes, considering the importance of suppressing the water layer formation on the surface of the electrode [86].

The distinct lasing settings used to fabricate the electrodes provided two different material composition surfaces and corresponding properties. Raman spectroscopy confirmed the well-established graphitic configuration for LIG-materials [47, 52] and was also used to compare the structures of both hydrophilic and hydrophobic surfaces, 1X-LIG and 2X-LIG (Fig. 2b). The three typical peaks, D, G, and 2D, roughly at 1350 cm^{-1}, 1580 cm^{-1}, and 2700 cm^{-1}, respectively, are obtained for materials based on graphene with a certain level of lattice defects. The D peak represents defects promoted by breaks and bends in sigma bonds, while the G

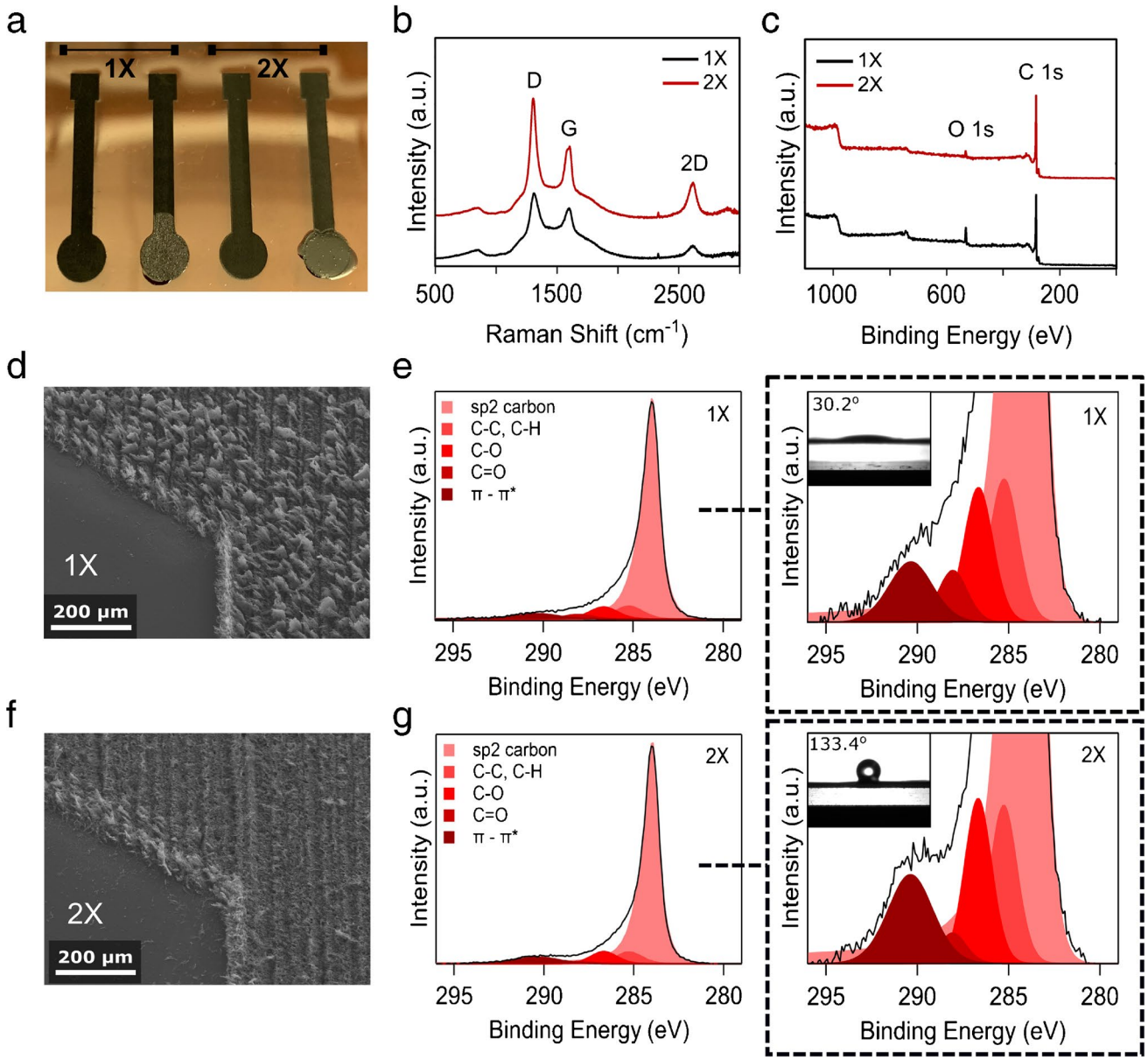

Fig. 2 **a** 1X-LIG and 2X-LIG before and after applying the ion-selective membrane. **b** Raman spectra comparing the three typical LIG peaks for both types of electrodes. **c** XPS survey exhibiting the clear decrease of oxygen content from 1X-LIG to 2X-LIG. SEM images of bare **d** 1X-LIG electrodes showing the difference in porosity compared with **f** 2X-LIG. **e** XPS spectra of bare electrodes showing the decrease of carbonyl groups from 1X-LIG to **g** 2X-LIG, and respective increase of π–π bonds, with insets providing a zoom of the five peaks and the respective contact angle measurements

peak is related to in-plane vibration of sp^2 carbon atoms, distinctive for graphitic material. In turn, the 2D peak is unique for graphene structures, which provides useful information about the stacking order and the number of graphene layers [87]. Thus, based on the values obtained for G and 2D peaks, it is possible to calculate the I_{2D}/I_G ratio regarding the number of graphene layers that were formed, that is, monolayer, bilayer, or multilayer. The 1X-LIG exhibited $I_{2D}/I_G \approx 0.25$, and similarly, the 2X-LIG exhibited $I_{2D}/I_G \approx 0.44$, which means both are based on multilayered graphene (with $I_{2D}/I_G < 1$) [88]. The higher this ratio, the better the quality of the graphene structure [89]. Previous works reported lower or similar I_{2D}/I_G ratios for LIG-materials, with values ranging from 0.30 to 0.44 [72, 90, 91]. The 2X-LIG displayed a higher D peak owing to additional bending in the carbon structures caused by the double lasing [53]. The I_D/I_G peaks for both LIG-materials were > 1, which is expected for LIG-materials and might also be attributed to the lasing process occurring in an uncontrolled atmosphere chamber [54]. These high D peaks might be related to the presence

of O_2 in the air, which provides an oxidative environment, thus generating rough edges and large pores, as previously described [54]. In addition, the XPS spectra showed a slight increase of π–π interactions, which are responsible for the carbon lattice stacking, after the second lasing. This proves that the laser-induction converts the sp^3 carbon structure mostly present in the PI into sp^2 type.

The surface chemical composition obtained from XPS showed that LIG materials are formed by carbon (C) and oxygen (O). Electrodes fabricated with one lasing step exhibited 89.96% of C and 10.04% of O, while 96.11% of C and 3.89% of O were observed after the second lasing. A reduction of ~ 2.5 times on the oxygen content after the second lasing (Fig. 2c) is directly related to the low wettability surface obtained, as the oxygen-containing functional groups exhibit high affinity with water. A similar work reported a reduction of ~ 3.9 times on the oxygen content after the second lasing, which was further related to the hydrophobic surface exhibiting a static water contact angle of ~143° [53]. The clear reduction of carbonyl groups is notable in Fig. 2e–g, which hinders hydrophilic interaction due to a lower incidence of hydrogen bonds (see Table S1 in Supplementary information). Additionally, the second lasing eliminates the vertically aligned structures (Fig. 2d–f) and creates a microporous surface that can be associated with a lower droplet adhesion force by increasing the fraction of liquid–air contact area on the surface (i.e., higher hydrophobicity) [53, 92].

Furthermore, the electrical conductivity was not significantly different ($p = 0.7720$) when comparing electrodes fabricated using both lasing methods, with a sheet resistance of 0.231 ± 0.033 kΩ sq^{-1} for 1X-LIG and 0.221 ± 0.046 kΩ sq^{-1} for 2X-LIG. These sheet resistance values are substantially lower than other published graphene-based materials, for instance, 15–20 kΩ sq^{-1} for LIG-based sensors fabricated with a low-cost UV-laser [72] and ~ 30 kΩ sq^{-1} for inkjet-printed graphene devices [93].

Electrochemical characterization

Cyclic voltammetric measurements of bare electrodes were performed to evaluate both LIG-electrodes and to estimate their electroactive surface area (ESA). Redox peaks were observed for both 1X- and 2X-LIG independent of the scan rate applied (Fig. 3a–b). The peak separation ranged from 264.82 to 896.18 mV for 1X-LIG and from 191.43 to 526.38 mV for 2X-LIG. The increase in potential peak separation at faster scan rates indicates a system with limitations in the electron transfer rate [94, 95]. Similarly, the Randles–Sevcik plots (Fig. S6b–c) demonstrate a linear increase in peak current with the square root of the scan rate for both LIG-electrodes, indicating a diffusion-controlled system [94, 96]. This behavior suggests a quasi-reversible system that is controlled by both mass and charge transfer [96, 97]. The calculated ESA for 1X-LIG was 49.84 ± 4.24 mm^2, representing 253.82% compared to the geometric area (19.63 mm^2). Alternatively, the 2X-LIG presented an ESA of 37.41 ± 0.97 mm^2, which is 190.52% higher than the geometric area. Higher ESA compared to the geometric area is consistently observed in LIG-based electrodes [73, 91, 98, 99]. The increase in ESA compared to the geometric area is attributed to the defect-rich highly porous 3D structure of the LIG, which increases the surface area and, consequently, creates more available sites for electron transfer during redox reactions [98, 99]. Despite the significantly higher ESA ($p = 0.0080$) presented by the 1X-LIG electrodes, the 2X-LIG was used for further sensing application because it exhibits a hydrophobic surface, which helps improve the stability of the sensor, as discussed previously and will be further demonstrated next.

Potential drifts, standard potential (E^0) reproducibility, and membrane delamination might be attributed to forming an aqueous film (water layer) between the selective membrane and the solid-contact interface [100, 101]. For this reason, water layer tests have become an important method to select and validate SC-ISEs. When an aqueous layer is formed, a longer time is required for the SC-ISE to reach the equilibrium potential, and substantial potential drift causes the need for frequent recalibration. Herein, SC-ISEs made with both 1X-LIG and 2X-LIG were subjected to two different solutions for a few hours, as previously described, and the potential was measured (Fig. 3c). The ISE based on 2X-LIG clearly exhibited a significant ($p = 0.0001$) lower potential drift, 397.6 ± 29.4 μV h^{-1}, compared to the 1X-LIG, 1262.5 ± 36.2 μV h^{-1}, after returning to the initial solution 1 mM $NaNO_2$ (section c in the Fig. 3c). This difference suggests that the hydrophobicity observed for 2X-LIG hinders the formation of a water layer, as previously reported [52] and contributes to a more stable potential. Moreover, the membrane applied onto 2X-LIG electrodes was thicker than the one applied to 1X-LIG (Fig. S5e) due to the membrane flowing over the 1X-LIG electrode stem, which possibly influenced the poor performance of the single-lasing electrodes as a recent study has reported that thin ion-selective membranes might exhibit anomalous potentiometric response because of changes in the water layer composition [102].

Another study to evaluate the potential stability was accomplished using constant current chronopotentiometry by applying a current of ± 1 nA, which is sufficient to polarize the surface of the electrode to calculate its capacitance [103] (Fig. 3d). The capacitances of both ISEs were calculated from Eq. S6. The potential drifts and capacitances were 11.7 ± 3.1 μV s^{-1} and 91.0 ± 23.7 μF for 1X-LIG, respectively, and 12.4 ± 1.0 μV s^{-1} and 88.3 ± 8.2 μF for 2X-LIG, which are very close to previous studies

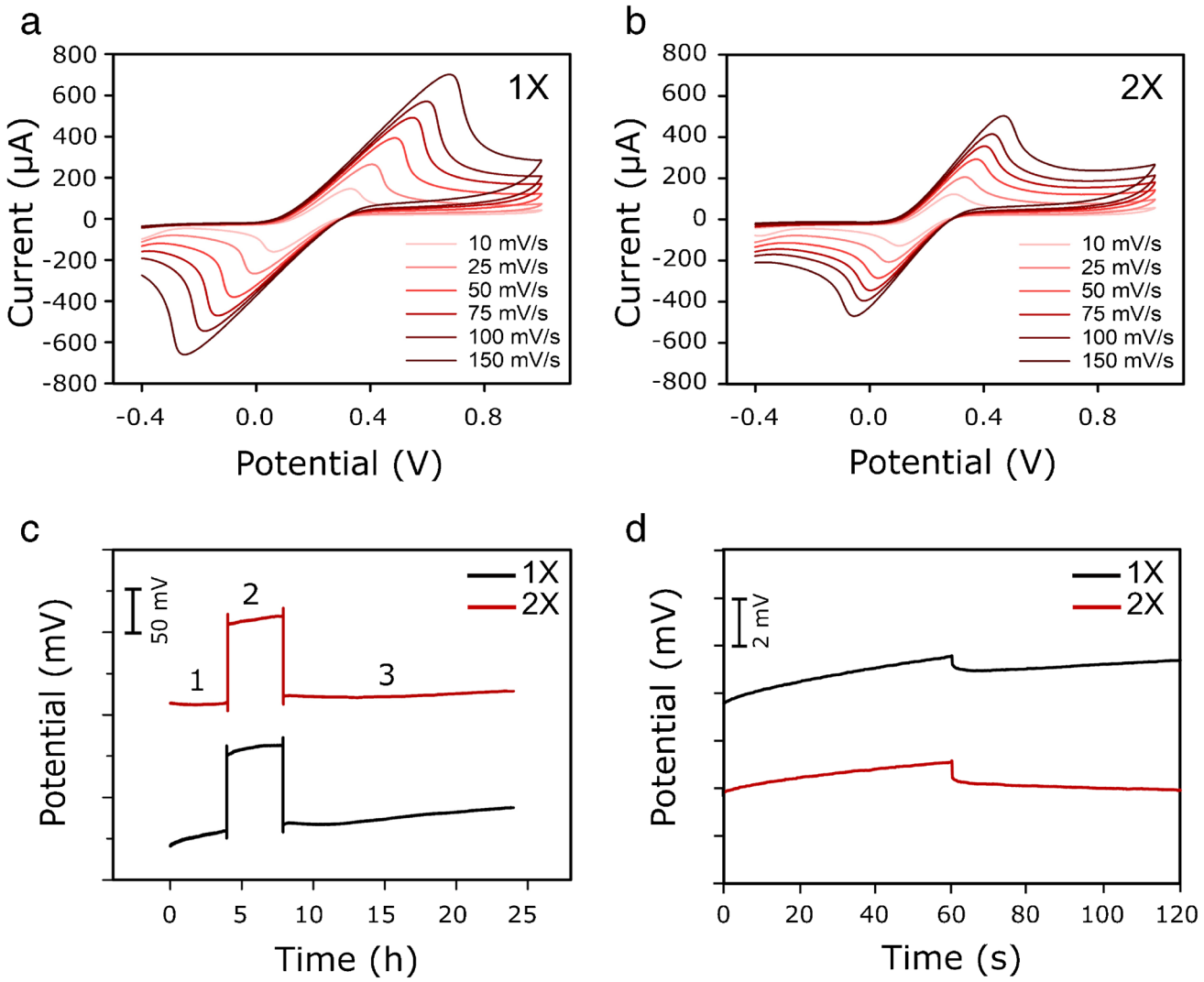

Fig. 3 **a**, **b** CV measurements for both 1X-LIG and 2X-LIG bare electrodes, respectively, at scan rates from 10 to 150 mV s^{-1}. **c** Water layer test for ISEs based on 1X-LIG and 2X-LIG, immersed in 1 mM $NaNO_2$ (1), 1 mM KCl (2), and back to 1 mM $NaNO_2$ (3) with 2X-LIG displaying lower potential drift. **d** Chronopotentiometry responses for both SC-ISEs based on 1X-LIG and 2X-LIG, with no significant difference observed for potential drift and capacitance values

with graphene-based ISEs, that obtained potential drifts in the range of 10 to 13 μV s^{-1}, and capacitances varying from 75 to 95 μF [52, 104]. No significant difference was observed for potential drifts ($p = 0.5808$) and capacitances ($p = 0.8425$), calculated from chronopotentiometry, when comparing ISEs made on hydrophilic and hydrophobic surfaces. However, the potential drift was notably higher for the hydrophilic SC-ISE observed from the water layer test. According to Eq. S6, the calculated capacitance is inversely proportional to the potential drift, which means higher capacitances are associated with more stable potential. As previously stated, one of the conditions for providing a stable and reliable SC-ISE is ideally nonpolarizable interfaces with high exchange current densities [105], which implies higher capacitances. This statement is relevant when considering the design of SC-ISEs for continuous ion monitoring. In this study, the capacitance values for both SC-ISEs are not significantly different, and they are in the range of other published graphene-based ISEs, but the 1-day measurement of potential drift (water layer test) displayed a significant difference for both, which demonstrates the utility of the hydrophobic LIG for ion sensing and in our particular case for nitrite ion sensing. Furthermore, the SC-ISE made with 1X-LIG exhibited a larger variability in potential when reading known concentrations of $NaNO_2$ compared to 2X-LIG (Fig. S3a–b and S4a–b). Thus, it implies less accuracy and consistency, displaying a higher standard deviation for the $NaNO_2$ measurement, which was also considered when choosing the hydrophobic LIG as a high-quality, stable sensor for potentiometric detection of nitrite.

Nitrite sensing

Open-circuit potentiometry was used to obtain calibration curves for nitrite SC-ISE fabricated from 1X- and 2X-LIG in DI water by incrementally increasing the nitrite levels in the electrochemical cell. The calibration curves demonstrated that both types of sensors performed following the Nernst equation (Eq. S7), which linearly relates the measured potential with the activity of a target ion, exhibiting sensitivities of 58.2 ± 2.0 and 59.5 ± 0.8 mV dec^{-1}, respectively (Fig. S3). The reproducibility of both sensors was evaluated considering the relative standard deviation values (RSD, Eq. S4) for the respective sensitivities, which are based on the slope of the linear calibration curve. The RSD values were 3.4% ($n = 4$) and 1.3% ($n = 4$) for sensors based on hydrophilic (1X-LIG) and hydrophobic (2X-LIG), respectively. These low values attest to the high reproducibility of the presented sensors. Additionally, once 2X-LIG was selected to perform the sensing analysis in real samples, 20 sensors were tested with sausage, ham, and bacon, and the RSD for their sensitivity was 5.51% ($n = 20$), indicating that even with an increase in the sample size, the RSD remains low.

Similar calibrations were performed in the presence of different salts (NaCl, NaH_2PO_4, and $NaNO_3$) to evaluate the effect of interfering ions commonly present in cured food (Fig. S4d). These calibrations enable the calculation of the selectivity coefficients (Eq. S5) for each tested ion and are reported in the last column of Table 1. These coefficients were relatively similar to a previously published work that also tested nitrite-ISE [106], where the $\log K^{pot}_{NO_2,i}$ for Cl^-, NO_3^-, and $H_2PO_4^-$ ranged from −2 to −3, showing that these three ions are not strictly discriminated by the nitrite ionophore [80] with $H_2PO_4^-$ showing the largest interference. Nonetheless, the results for nitrite determination showed that interfering ions did not negatively affect the sensor's performance in food samples.

Previous studies have developed sensors that can detect nitrite at very low detection limits, often in the nanomolar range (Table 2); however, not only these sensors require noble metals and other expensive materials to fabricate, but also need extensive sample pre-treatments. Most of them show a limited detection range regarding the upper limit imposed by federal regulations in the USA [13] ($\approx 4 \times 10^{-3}$ M or 200 ppm of nitrite), which results in the need of several dilutions and sample preparation. Furthermore, nitrite sensors based on potentiometric techniques are not very common (Table 2), showing an opportunity for implementing this little-explored approach. As usual for potentiometric techniques, the sensor developed herein can detect nitrite in a wide range that spans four orders of magnitude (Fig. 4a), 0.33 to 4600 ppm, far exceeding the federally set limit for cured meats as well as for drinking water (1 ppm according to U.S. Environmental Protection Agency) [14]. Additionally, the developed sensing method does not require sample dilutions or pre-treatments, avoiding major intrinsic errors, and exhibits a relative low cost per sensor, approximately US$ 1.20, considering only material expenses.

A review paper published in 2019 compared more than a hundred graphene-based electrochemical sensors for nitrite detection, and all of them used either voltammetry or amperometry as the electrochemical technique [78]. In many of these works, in addition to the excessive and laborious steps to obtain the modified electrodes, the detection ranges were not as wide as expected, except for a few cases where they were within the regulated levels for food but only tested in water sources. The ability to address all existing challenges regarding the stability and reliability of the measured potential, solid contact surface structure, and selectivity, the present nitrite sensor, based on a potentiometric technique, offers an alternative method with an unusual approach and outstanding sensing performance.

Before measuring the potential of food extracts, the sensors were calibrated by measuring the emf of six different nitrite solutions with known concentrations ranging from 10 to 10,000 µM (Fig. S4e). Average measurement time was 5 min, and response time at 95% of the stead-state signal (t95) was 9 s. The emf obtained for each sensor corroborated with the known nitrite concentrations by applying it to the linear equations obtained from the calibrations. A correlation relating expected and experimental values are shown in Fig. 4c, where the experimental values are notably close to the expected ones, especially at higher concentrations, exhibiting a mean absolute percentage error (MAPE) of 6.7% (Eq. S8). These MAPE

Table 1 Electrochemical performance of nitrite SC-ISE based on 2X-LIG and selectivity coefficients at 1 mM interfering-ion concentration ($n = 4$). Values given are mean ± standard deviations

Sensitivity (mV/dec)	LOD (µM)	Range of detection (M)	Standard potential E^o (mV)	Response time (s)	Selectivity coefficient	
−59.5 ± 0.8	7.2 ± 3.6	10^{-5} to 10^{-1}	−13.1 ± 4.0	9 ± 2	$\log K^{pot}_{i,Cl^-}$	−1.74 ± 0.05
					$\log K^{pot}_{i,(H_2PO_4)^-}$	−3.17 ± 0.02
					$\log K^{pot}_{i,NO_3^-}$	−1.39 ± 0.05

Table 2 Comparison of recently published reports on electrochemical nitrite sensors

Transducer	Functionalization	Electrochemical technique	LOD (μM)	Detection range (M)	Sample	Ref
GCE	Hemoglobin/AuNPs-CMK-8/GC	DPV	0.0021	5×10^{-9} to 10^{-3}	Extract of meat	[107]
GCE	FeT4MPyP/CuTSP	DPV	0.1	5×10^{-7} to 7.5×10^{-6}	Extract of sausage and vegetables	[108]
GCE	Cu/MWCNT/RGO	SWV	0.03	10^{-7} to 7.5×10^{-5}	Extract of sausage, salami, and cheese	[84]
GCE	TiO_2–$Ti_3C_2T_X$ nanohybrid/CTAB/CS	DPV	0.85	3×10^{-6} to 1.25×10^{-3}	Water and milk	[109]
Au-SPE	2-ATP/PVA/GA/AuNPs	DPV	4	~10^{-5} to 10^{-3}	Exhaled breath condensate	[110]
GCE	Au–HNTs–GO	Amperometry	0.03	10^{-7} to 6.2×10^{-2}	Tap water	[111]
GCE	Fe-BZIM/Nafion	CV and CP	< 1	10^{-6} to 10^{-4}	-	[112]
GCE	GO-MWCNT-Pt/Mb	Amperometry	0.93	10^{-6} to 1.2×10^{-2}	Rain, river, and tap water	[113]
GCE	MWCNT/nitrite-selective membrane	Potentiometry	0.6	10^{-6} to 10^{-2}	Seawater	[114]
LIG	Bare-LIG	DPV	0.8	5×10^{-6} to 4.5×10^{-4}	Tap water and pickle water	[115]
LIG	CS	DPV	0.9	2×10^{-6} to 10^{-3}	Tap water and lake water	[116]
LIG	MWCNT-AuNPs	SWV	0.9	10^{-5} to 1.4×10^{-4}	Tap water and PBS	[117]
LIG	ION-RGO	DPV	7.21	10^{-5} to 4×10^{-4}	PBS buffer	[118]
LIG	Bare-LIG	DPV	0.27	10^{-5} to 7×10^{-5}	Buffered solution	[119]
LIG	Nitrite-selective membrane	OCP	7.2	10^{-5} to 10^{-1}	Extract of cured meat	**This work**

ATP, aminothiophenol; *PVA*, polyvinyl alcohol; *GA*, glutaraldehyde; *SPE*, screen-printed electrode; *HNTs*, natural halloysite nanotubes; *GO*, graphene oxide; *AuNPs*, gold nanoparticles; *CMK-8*, mesoporous carbon composites; *CP*, chronopotentiometry; *CS*, chitosan; *CTAB*, hexadecyl trimethyl ammonium bromide; *CuTSP*, copper tetrasulfonated phthalocyanine; *CV*, cyclic voltammetry; *DPV*, differential pulse voltammetry; *FeT4MPyP*, iron (III) tetra-(N-methyl-4-pyridyl)-porphyrin; *GCE*, glassy carbon electrode; *LIG*, laser-induced graphene; *Mb*, myoglobin; *ION-RGO*, iron oxide nanoparticle with reduced graphene oxide; *MWCNT*, multiwall carbon nanotubes; *OCP*, open-circuit potentiometry; *RGO*, reduced graphene oxide; *SWV*, Square wave voltammetry.

results are indicative of the high reliability of the developed method. The application of MAPE as a loss function for regression analysis is relevant both from practical and theoretical points of view because of the existence of an optimal (real) model that allows for verification of empirical values, where the consistency can be proved [120].

To validate the method, a standard spectrophotometric assay that uses Griess reagents for nitrite detection [83, 121] was compared to the potentiometric response obtained with the developed nitrite sensor. There were no significant differences for samples analysis of sausage ($p=0.2369$), ham ($p=0.3025$), and bacon ($p=0.6141$) when comparing both potentiometric and spectrophotometric techniques (Fig. 4d). For the Griess method, a linear calibration curve was obtained by measuring the absorbance of solutions with different nitrite concentrations (Fig. 4b). In this work, all food samples tested complied with federal legislation, with nitrite levels below 200 ppm. Based on the present method and the Griess standard method, respectively, the sausage samples exhibited 3.8 ± 1.1 ppm and 4.7 ± 0.9 ppm, ham samples exhibited 23.5 ± 2.4 ppm and 21.5 ± 3.0 ppm, and bacon samples exhibited 31.2 ± 4.6 and 29.7 ± 2.7 ppm of nitrite. It is relevant to mention that these sensors can be used multiple times to test different samples in sequence. Additional studies should be performed in future works to precisely describe how many times these sensors can be used and their shelf-life under storage. Furthermore, there is a growing interest in using SC-ISE sensors for continuous measurements for in-field applications, and in this case, it would be desirable to add other conductive materials, such as metal nanoparticles or conductive polymers to the LIG surface to increase capacitance that could improve potential stability, and consequently reduce potential drift [122, 123].

Conclusions

This work reports the successful development of a solid-contact-ion selective electrode (SC-ISE) by utilizing a laser-induced graphene (LIG) platform capable of monitoring

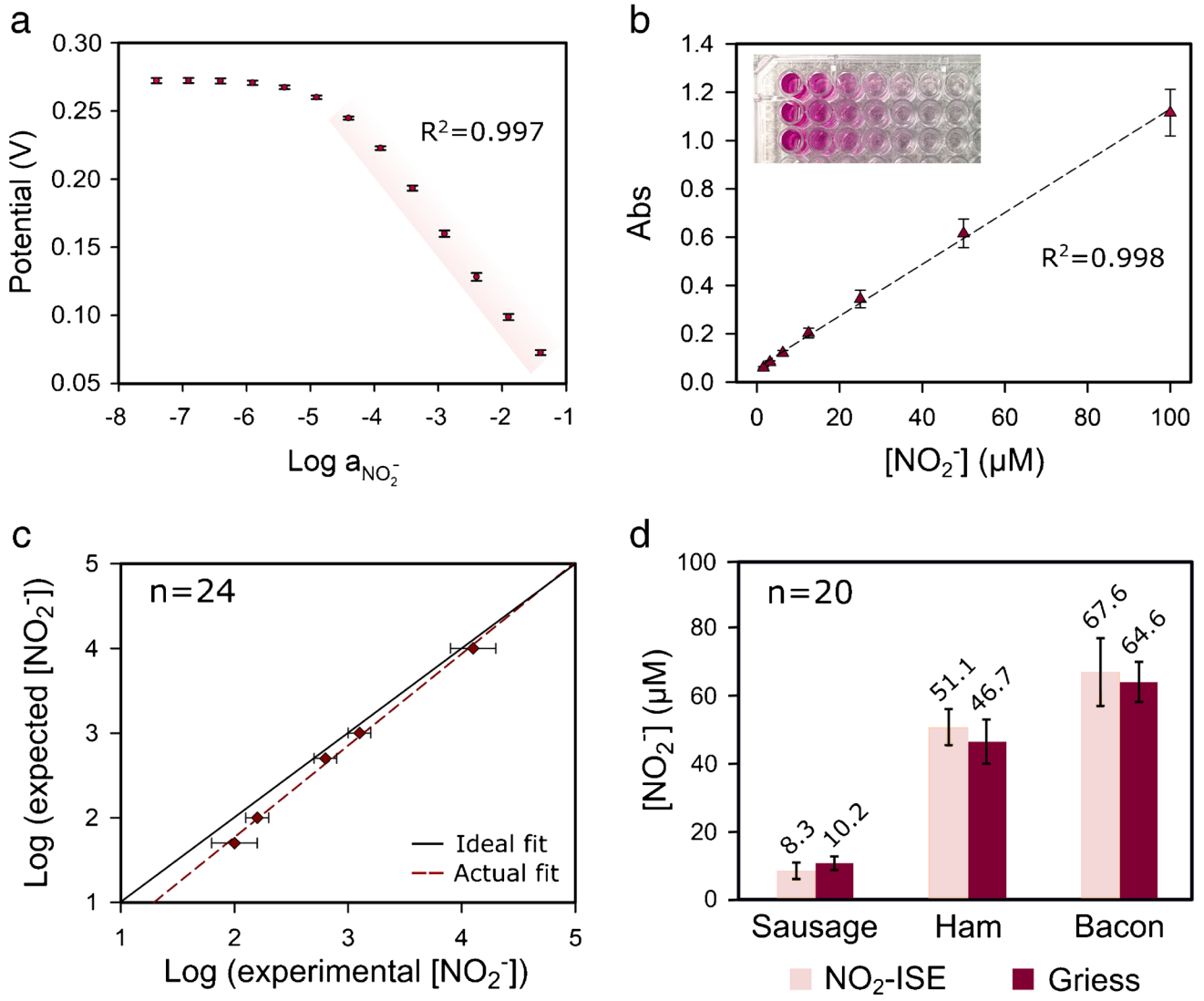

Fig. 4 **a** Calibration curve with half-log step additions ranging from 10^{-7} to 10^{-1} M of $NaNO_2$, showing a highlighted linear range, $n=4$. **b** Calibration curve obtained by measuring the absorbance of different nitrite concentrations using the Griess reagents kit, inlet: triplicate of $NaNO_2$ (100, 50, 25, 12.5, 6.25, 3.125, 1.5625 μM) reacting with these reagents. **c** Comparison between expected and experimental potential readings at five different nitrite concentrations 50, 100, 500, 10^3, and $10.^4$ μM, exhibiting a slight offset from the ideal correlation. **d** Validation of the developed method compared to the standard method, with no significant differences for all three types of meat, units in μM ($\alpha<0.05$)

nitrite levels in cured food products over regulatory compliance ranges. The hydrophobic LIG-electrodes proved more suitable as SC-ISE than the hydrophilic LIG because it hindered the formation of a water layer with significantly lower potential drift, contributing to a more stable potential. These sensors exhibited a wide linear range spanning four orders of magnitude of nitrite concentration (10^{-5} to 10^{-1} M), near-theoretical sensitivity of 59.5 mV/dec, and a considerably low detection limit when compared to the limits imposed by federal regulations. These analytical characteristics resemble or exceed previous nitrite sensing studies [78] and far exceed the federal limit of ~ 200 ppm in cured meat [13]. Importantly, other ions commonly found in cured meats did not prevent the sensors from detecting the target ion. In just 5 min, the ISE-LIG sensor could quantitatively detect nitrite in extracts of cured meats with no significant difference from the standard method. In summary, the ISE-LIG sensor not only demonstrates a sensitive and rapid method for nitrite monitoring but also has the potential for widespread adoption given its fabrication using inexpensive and high-throughput laser induction technique that eliminates multiple preparation steps and does not require modification of electrodes with nanomaterials as in previous reports [84, 107, 110]. Furthermore, this sensing platform can be easily

modified for many ions relevant to human health, precision agriculture, surface and drinking water quality, and food contaminant monitoring, which suggests its widespread use in future potentiometric sensing applications.

Supplementary Information The online version contains supplementary material available at https://doi.org/10.1007/s00604-022-05615-9.

Acknowledgements We would like to thank Joshua Jarnagin and Camden Jackson for their help with the experiments.

Funding This study received funding support from the National Institute of Food and Agriculture, U.S. Department of Agriculture, award numbers 2020–67021-31375 and 2018–67016-27578 awarded as a Center of Excellence, and the National Science Foundation under award numbers NSF CMMI-2037026 and NSF PFI-2141198.

Data availability The data presented in this study are available on request from the corresponding authors.

Declarations

Competing interests The authors declare no competing interests.

References

1. Jo K, Lee S, Yong HI, Choi YS, Jung S (2020) Nitrite sources for cured meat products. Lwt 129(May):109583. https://doi.org/10.1016/j.lwt.2020.109583
2. Honikel KO (2008) The use and control of nitrate and nitrite for the processing of meat products. Meat Sci 78(1–2):68–76. https://doi.org/10.1016/j.meatsci.2007.05.030
3. Parthasarathy DK, Bryan NS (2012) Sodium nitrite: the "Cure" for nitric oxide insufficiency. Meat Sci 274–279. https://doi.org/10.1016/j.meatsci.2012.03.001
4. MacDougall DB (1982) Changes in the colour and opacity of meat. Food Chem 9(1–2):75–88. https://doi.org/10.1016/0308-8146(82)90070-X
5. Macdougall DB, Mottram DS, Rhodes DN (1975) Contribution of nitrite and nitrate to the colour and flavour of cured meats. J Sci Food Agric 26(11):1743–1754. https://doi.org/10.1002/jsfa.2740261117
6. Froehlich DA, Gullett EA, Usborne WR (1983) Effect of nitrite and salt on the color, flavor and overall acceptability of ham. J Food Sci 48(1):152–154. https://doi.org/10.1111/j.1365-2621.1983.tb14811.x
7. Reddy D, Lancaster JR, Cornforth DP (1983) Nitrite inhibition of clostridium botulinum: electron spin resonance detection of iron-nitric oxide complexes. Science (1979) 221(4612):769–770. https://doi.org/10.1126/science.6308761
8. Kilfoy BA, Zhang Y, Park Y, Holford TR, Schatzkin A, Hollenbeck A, Ward MH (2011) Dietary nitrate and nitrite and the risk of thyroid cancer in the NIH-AARP diet and health study. Int J Cancer 129(1):160–172. https://doi.org/10.1002/ijc.25650
9. Kalaycloğlu Z, Erim FB (2019) Nitrate and nitrites in foods: worldwide regional distribution in view of their risks and benefits. J Agric Food Chem 67(26):7205–7222. https://doi.org/10.1021/acs.jafc.9b01194
10. De Mey E, De Klerck K, De Maere H, Dewulf L, Derdelinckx G, Peeters MC, Fraeye I, Vander Heyden Y, Paelinck H (2014) The occurrence of N-nitrosamines, residual nitrite and biogenic amines in commercial dry fermented sausages and evaluation of their occasional relation. Meat Sci 96(2):821–828. https://doi.org/10.1016/j.meatsci.2013.09.010
11. Michaud DS, Holick CN, Batchelor TT, Giovannucci E, Hunter DJ (2009) Prospective study of meat intake and dietary nitrates, nitrites, and nitrosamines and risk of adult glioma. Am J Clin Nutr 90(3):570–577. https://doi.org/10.3945/ajcn.2008.27199
12. Lijinsky W (1976) Health problems associated with nitrites and nitrosamines. Ambio 5(2):67–72
13. USDA-FSIS (1999) 9 CFR – Animals and animal products; Food Safety and Inspection Service. Department of Agriculture, United States, pp 565–591
14. Environmental Protection Agency (1975) 40 CFR – protection of environment; Authenticated U.S. Governement Information, United States
15. Singh P, Singh MK, Beg YR, Nishad GR (2019) A review on spectroscopic methods for determination of nitrite and nitrate in environmental samples. Talanta. Elsevier B.V, pp 364–381. https://doi.org/10.1016/j.talanta.2018.08.028
16. Moorcroft MJ, Davis J, Compton RG (2001) Detection and determination of nitrate and nitrite: a review. Talanta 54:785–803. https://doi.org/10.1016/S0039-9140(01)00323-X
17. Wang QH, Yu LJ, Liu Y, Lin L, Lu RG, Zhu JP, He L, Lu ZL (2017) Methods for the detection and determination of nitrite and nitrate: a review. Talanta 165:709–720. https://doi.org/10.1016/j.talanta.2016.12.044
18. Ayala A, Leal LO, Ferrer L, Cerdà V (2012) Multiparametric automated system for sulfate, nitrite and nitrate monitoring in drinking water and wastewater based on sequential injection analysis. Microchem J 100(1):55–60. https://doi.org/10.1016/j.microc.2011.09.004
19. He L, Zhang K, Wang C, Luo X, Zhang S (2011) Effective indirect enrichment and determination of nitrite ion in water and biological samples using ionic liquid-dispersive liquid-liquid microextraction combined with high-performance liquid chromatography. J Chromatogr A 1218(23):3595–3600. https://doi.org/10.1016/j.chroma.2011.04.014
20. Helaleh MIH, Korenaga T (2000) Ion chromatographic method for simultaneous determination of nitrate and nitrite in human saliva. J Chromatogr B 744:433–437. https://doi.org/10.1016/S0378-4347(00)00264
21. Kodamatani H, Yamazaki S, Saito K, Komatsu Y, Tomiyasu T (2011) Rapid method for simultaneous determination of nitrite and nitrate in water samples using short-column ion-pair chromatographic separation, photochemical reaction, and chemiluminescence detection. Anal Sci 27:187–192
22. Erdogan BY, Onar AN (2011) Determination of nitrates, nitrites and oxalates in Kale and Sultana Pea by capillary electrophoresis. J Anim Vet Adv 10(15):2051–2057
23. Li D, Ma Y, Duan H, Deng W, Li D (2018) Griess reaction-based paper strip for colorimetric/fluorescent/SERS triple sensing of nitrite. Biosens Bioelectron 99:389–398. https://doi.org/10.1016/j.bios.2017.08.008
24. Xiang G, Wang Y, Zhang H, Fan H, Fan L, He L, Jiang X, Zhao W (2018) Carbon dots based dual-emission silica nanoparticles as ratiometric fluorescent probe for nitrite determination in food samples. Food Chem 260:13–18. https://doi.org/10.1016/j.foodchem.2018.03.150
25. Liu QH, Yan XL, Guo JC, Wang DH, Li L, Yan FY, Chen LG (2009) Spectrofluorimetric determination of trace nitrite with a novel fluorescent probe. Spectrochim Acta A Mol Biomol Spectrosc 73(5):789–793. https://doi.org/10.1016/j.saa.2009.03.018
26. Feng D, Zhang Y, Shi W, Li X, Ma H (2010) A simple and sensitive method for visual detection of phosgene based on the aggregation of gold nanoparticles. Chem Commun 46(48):9203–9205. https://doi.org/10.1039/c0cc02703k

27. Daniel WL, Han MS, Lee JS, Mirkin CA (2009) Colorimetric nitrite and nitrate detection with gold nanoparticle probes and kinetic end points. J Am Chem Soc 131(18):6362–6363. https://doi.org/10.1021/ja901609k
28. Li J, Li Q, Lu C, Zhao L (2011) Determination of nitrite in tap waters based on fluorosurfactant-capped gold nanoparticles-enhanced chemiluminescence from carbonate and peroxynitrous acid. Analyst 136(11):2379–2384. https://doi.org/10.1039/c0an00918k
29. Ensafi AA, Amini M (2010) A highly selective optical sensor for catalytic determination of ultra-trace amounts of nitrite in water and foods based on brilliant cresyl blue as a sensing reagent. Sens Actuators B Chem 147(1):61–66. https://doi.org/10.1016/j.snb.2010.03.014
30. Liu X, Guo L, Cheng L, Ju H (2009) Determination of nitrite based on its quenching effect on anodic electrochemiluminescence of CdSe quantum dots. Talanta 78(3):691–694. https://doi.org/10.1016/j.talanta.2008.12.035
31. Latimer GW (2016) Official methods of analysis of AOAC international, vol. II, 20th edn. AOAC International, Gaithersburg
32. Raccichini R, Varzi A, Passerini S, Scrosati B (2015) The role of graphene for electrochemical energy storage. Nat Mater 14(3):271–279. https://doi.org/10.1038/nmat4170
33. Tang L, Wang Y, Li Y, Feng H, Lu J, Li J (2009) Preparation, structure, and electrochemical properties of reduced graphene sheet films. Adv Funct Mater 19(17):2782–2789. https://doi.org/10.1002/adfm.200900377
34. Pumera M (2011) Graphene in biosensing - review. Mater Today 14(7–8):308–315
35. Baig N, Saleh TA (2018) Electrodes modified with 3D graphene composites: a review on methods for preparation, properties and sensing applications. Microchimica Acta. Springer-Verlag Wien. https://doi.org/10.1007/s00604-018-2809-3
36. Zhang Z, Xiao F, Qian L, Xiao J, Wang S, Liu Y (2014) Facile synthesis of 3D MnO2-graphene and carbon nanotube-graphene composite networks for high-performance, flexible, all-solid-state asymmetric supercapacitors. Adv Energy Mater 4(10). https://doi.org/10.1002/aenm.201400064
37. Thomas T, Agarwal A (2021) A facile and scalable approach in the fabrication of tailored 3d graphene foam via freeze drying. Materials 14(4):1–18. https://doi.org/10.3390/ma14040864
38. Jiang C, Zhao B, Cheng J, Li J, Zhang H, Tang Z, Yang J (2015) Hydrothermal synthesis of Ni(OH)2 nanoflakes on 3D graphene foam for high-performance supercapacitors. Electrochim Acta 173:399–407. https://doi.org/10.1016/j.electacta.2015.05.081
39. Das SR, Nian Q, Cargill AA, Hondred JA, Ding S, Saei M, Cheng GJ, Claussen JC (2016) Nanostructured inkjet printed graphene: via UV-pulsed laser irradiation enables paper-based electronics and electrochemical devices. Nanoscale 8(35):15870–15879. https://doi.org/10.1039/c6nr04310k
40. Moya A, Gabriel G, Villa R, Javier del Campo F (2017) Inkjet-printed electrochemical sensors. Current Opinion in Electrochemistry. Elsevier B.V pp 29–39. https://doi.org/10.1016/j.coelec.2017.05.003
41. Huang X, Leng T, Zhu M, Zhang X, Chen J, Chang K, Aqeeli M, Geim AK, Novoselov KS, Hu Z (2015) Highly flexible and conductive printed graphene for wireless wearable communications applications. Sci Rep 5. https://doi.org/10.1038/srep18298
42. Browne MP, Novotný F, Sofer Z, Pumera M (2018) 3D printed graphene electrodes' electrochemical activation. ACS Appl Mater Interfaces 10(46):40294–40301. https://doi.org/10.1021/acsami.8b14701
43. Fu K, Wang Y, Yan C, Yao Y, Chen Y, Dai J, Lacey S, Wang Y, Wan J, Li T, Wang Z, Xu Y, Hu L (2016) Graphene oxide-based electrode inks for 3D-printed lithium-ion batteries. Adv Mater 28(13):2587–2594. https://doi.org/10.1002/adma.201505391
44. Secor EB, Prabhumirashi PL, Puntambekar K, Geier ML, Hersam MC (2013) Inkjet printing of high conductivity, flexible graphene patterns. J Phys Chem Lett 4(8):1347–1351. https://doi.org/10.1021/jz400644c
45. Secor EB, Ahn BY, Gao TZ, Lewis JA, Hersam MC (2015) Rapid and versatile photonic annealing of graphene inks for flexible printed electronics. Adv Mater 27(42):6683–6688. https://doi.org/10.1002/adma.201502866
46. Schumann M, Sauerbrey R, Smayling MC (1991) Permanent increase of the electrical conductivity of polymers induced by ultraviolet laser radiation. Appl Phys Lett 58(4):428–430. https://doi.org/10.1063/1.104624
47. Lin J, Peng Z, Liu Y, Ruiz-Zepeda F, Ye R, Samuel ELG, Yacaman MJ, Yakobson BI, Tour JM (2014) Laser-induced porous graphene films from commercial polymers. Nat Commun 5:1–8. https://doi.org/10.1038/ncomms6714
48. Chyan Y, Ye R, Li Y, Singh SP, Arnusch CJ, Tour JM (2018) Laser-induced graphene by multiple lasing: toward electronics on cloth, paper, and food. ACS Nano 12(3):2176–2183. https://doi.org/10.1021/acsnano.7b08539
49. Huang J, Liu Y, You T (2010) Carbon nanofiber based electrochemical biosensors: a review. Anal Methods 2(3):202–211. https://doi.org/10.1039/b9ay00312f
50. Wanjari VP, Reddy AS, Duttagupta SP, Singh SP (2022) Laser-induced graphene-based electrochemical biosensors for environmental applications: a perspective. Environmental Science and Pollution Research. Springer Science and Business Media Deutschland GmbH. https://doi.org/10.1007/s11356-022-21035-x
51. Mamleyev,ER, Heissler S, Nefedov A, Weidler PG, Nordin N, Kudryashov VV, Länge K, MacKinnon N, Sharma S (2019) Laser-induced hierarchical carbon patterns on polyimide substrates for flexible urea sensors. npj Flex Electron 3 (1). https://doi.org/10.1038/s41528-018-0047-8
52. Hjort RG, Soares RRA, Li J, Jing D, Hartfiel L, Chen B, van Belle B, Soupir M, Smith E, Mclamore E, Claussen JC, Gomes CL (2022) Hydrophobic laser induced graphene potentiometric ion selective electrodes for nitrate sensing. Microchimica Acta 189(122):1–11. https://doi.org/10.1007/s00604-022-05233-5
53. Chen B, Johnson ZT, Sanborn D, Hjort RG, Garland NT, Soares RRA, van Belle B, Jared N, Li J, Jing D, Smith EA, Gomes CL, Claussen JC (2022) Tuning the structure, conductivity, and wettability of laser-induced graphene for multiplexed open microfluidic environmental biosensing and energy storage devices. ACS Nano 16:15–28. https://doi.org/10.1021/acsnano.1c04197
54. Li Y, Luong DX, Zhang J, Tarkunde YR, Kittrell C, Sargunaraj F, Ji Y, Arnusch CJ, Tour JM (2017) Laser-induced graphene in controlled atmospheres: from superhydrophilic to superhydrophobic surfaces. Adv Mater 29(27):1–8. https://doi.org/10.1002/adma.201700496
55. Nasser J, Lin J, Zhang L, Sodano HA (2020) Laser induced graphene printing of spatially controlled super-hydrophobic/hydrophilic surfaces. Carbon N Y 162:570–578. https://doi.org/10.1016/j.carbon.2020.03.002
56. Kaur S, Mager D, Korvink JG, Islam M (2021) Unraveling the dependency on multiple passes in laser-induced graphene electrodes for supercapacitor and H2O2 sensing. Mater Sci Energy Technol 4:407–412. https://doi.org/10.1016/j.mset.2021.09.004
57. Criscuolo F, Hanitra MIN, Taurino I, Carrara S, De Micheli G (2021) All-solid-state ion-selective electrodes: a tutorial for correct practice. IEEE Sens J 21(20):22143–22154. https://doi.org/10.1109/JSEN.2021.3099209
58. Shao Y, Ying Y, Ping J (2020) Recent advances in solid-contact ion-selective electrodes: functional materials,

transduction mechanisms, and development trends. Chem Soc Rev 49(13):4405–4465. https://doi.org/10.1039/c9cs00587k
59. Zhao G, Liang R, Wang F, Ding J, Qin W (2019) An all-solid-state potentiometric microelectrode for detection of copper in coastal sediment pore water. Sens Actuators B Chem 279:369–373. https://doi.org/10.1016/j.snb.2018.09.125
60. Xu H, Wang Y, Luo Z, Pan Y (2013) A miniature all-solid-state calcium electrode applied to in situ seawater measurement. Meas Sci Technol 24 (12). https://doi.org/10.1088/0957-0233/24/12/125105
61. Zhao G, Ding J, Qin W (2019) Fine-scale in-situ measurement of lead ions in coastal sediment pore water based on an all-solid-state potentiometric microsensor. Anal Chim Acta 1073:39–44. https://doi.org/10.1016/j.aca.2019.04.059
62. Anastasova-Ivanova S, Mattinen U, Radu A, Bobacka J, Lewenstam A, Migdalski J, Danielewski M, Diamond D (2010) Development of miniature all-solid-state potentiometric sensing system. Sens Actuators B Chem 146(1):199–205. https://doi.org/10.1016/j.snb.2010.02.044
63. Malon A, Radu A, Qin W, Qin Y, Ceresa A, Maj-Zurawska M, Bakker E, Pretsch E (2003) Improving the detection limit of anion-selective electrodes: an iodide-selective membrane with a nanomolar detection limit. Anal Chem 75(15):3865–3871. https://doi.org/10.1021/ac026454r
64. Kim Y, Amemiya S (2008) Stripping analysis of nanomolar perchlorate in drinking water with a voltammetric ion-selective electrode based on thin-layer liquid membrane. Anal Chem 80(15):6056–6065. https://doi.org/10.1021/ac8008687
65. Zhai J, Zhang Y, Zhao D, Kou L, Zhao G (2022) In vivo monitoring of calcium ions in rat cerebrospinal fluid using an all-solid-state acupuncture needle based potentiometric microelectrode. Anal Chim Acta 1191:339209. https://doi.org/10.1016/j.aca.2021.339209
66. Kim YS, Ha Y, Sim J, Suh M, Lee Y (2016) Location-dependent sensing of nitric oxide and calcium ions in living rat kidney using an amperometric/potentiometric dual microsensor. Analyst 141(1):297–304. https://doi.org/10.1039/c5an01804h
67. Odijk M, van der Wouden EJ, Olthuis W, Ferrari MD, Tolner EA, van den Maagdenberg AMJM, van den Berg A (2015) Microfabricated solid-state ion-selective electrode probe for measuring potassium in the living rodent brain: compatibility with DC-EEG recordings to study spreading depression. Sens Actuators B Chem 207(PB):945–953. https://doi.org/10.1016/j.snb.2014.06.138
68. Parrilla M, Cuartero M, Padrell Sánchez S, Rajabi M, Roxhed N, Niklaus F, Crespo GA (2019) Wearable all-solid-state potentiometric microneedle patch for intradermal potassium detection. Anal Chem 91(2):1578–1586. https://doi.org/10.1021/acs.analchem.8b04877
69. Novell M, Guinovart T, Blondeau P, Rius FX, Andrade FJ (2014) A paper-based potentiometric cell for decentralized monitoring of Li levels in whole blood. Lab Chip 14(7):1308–1314. https://doi.org/10.1039/c3lc51098k
70. van de Velde L, d'Angremont E, Olthuis W (2016) Solid contact potassium selective electrodes for biomedical applications—a review. Talanta. Elsevier B.V., pp 56–65. https://doi.org/10.1016/j.talanta.2016.06.050
71. Lindner E, Gyurcsányi RE (2009) Quality control criteria for solid-contact, solvent polymeric membrane ion-selective electrodes. J Solid State Electrochem 13(1):51–68. https://doi.org/10.1007/s10008-008-0608-1
72. Garland NT, McLamore ES, Cavallaro ND, Mendivelso-Perez D, Smith EA, Jing D, Claussen JC (2018) Flexible laser-induced graphene for nitrogen sensing in soil. ACS Appl Mater Interfaces 10(45):39124–39133. https://doi.org/10.1021/acsami.8b10991
73. Kucherenko IS, Sanborn D, Chen B, Garland N, Serhan M, Forzani E, Gomes C, Claussen JC (2020) Ion-selective sensors based on laser-induced graphene for evaluating human hydration levels using urine samples. Adv Mater Technol 5(6):1–9. https://doi.org/10.1002/admt.201901037
74. Kucherenko IS, Chen B, Johnson Z, Wilkins A, Sanborn D, Figueroa-Felix N, Mendivelso-Perez D, Smith EA, Gomes C, Claussen JC (2021) Laser-induced graphene electrodes for electrochemical ion sensing, pesticide monitoring, and water splitting. Anal Bioanal Chem 413:6201–3212. https://doi.org/10.1007/s00216-021-03519-w/Published
75. Lee CW, Jeong SY, Kwon YW, Lee JU, Cho SC, Shin BS (2016) Fabrication of laser-induced graphene-based multifunctional sensing platform for sweat ion and human motion monitoring. Sens Actuators A Phys 334. https://doi.org/10.1016/j.sna.2021.113320
76. Yang Y, Song Y, Bo X, Min J, Pak OS, Zhu L, Wang M, Tu J, Kogan A, Zhang H, Hsiai TK, Li Z, Gao W (2020) A laser-engraved wearable sensor for sensitive detection of uric acid and tyrosine in sweat. Nat Biotechnol 38(2):217–224. https://doi.org/10.1038/s41587-019-0321-x
77. Kozub BR, Rees NV, Compton RG (2010) Electrochemical determination of nitrite at a bare glassy carbon electrode; why chemically modify electrodes? Sens Actuators B Chem 143(2):539–546. https://doi.org/10.1016/j.snb.2009.09.065
78. Li G, Xia Y, Tian Y, Wu Y, Liu J, He Q, Chen D (2019) Review—recent developments on graphene-based electrochemical sensors toward nitrite. J Electrochem Soc 166(12):B881–B895. https://doi.org/10.1149/2.0171912jes
79. Radu A, Meir AJ, Bakker E (2004) Dynamic diffusion model for tracing the real-time potential response of polymeric membrane ion-selective electrodes. Anal Chem 76(21):6402–6409. https://doi.org/10.1021/ac049348t
80. Bakker E (1996) Determination of improved selectivity coefficients of polymer membrane ion-selective electrodes by conditioning with a discriminated ion. J Electrochem Soc 143(4):83–85
81. Umezawa Y, Umezawa K, Bühlmann P, Hamada N, Aoki H, Nakanishi J, Sato M, Xiao KP, Nishimura Y (2002) Potentiometric selectivity coefficients of ion-selective electrodes, part II. Inorganic Anions Pure Appl Chem 74(6):923–994
82. Cunningham AJ (1998) Introduction to bioanalytical sensors. Wiley, New York
83. Miranda KM, Espey MG, Wink DA (2001) A rapid, simple spectrophotometric method for simultaneous detection of nitrate and nitrite. Nitric Oxide 5(1):62–71. https://doi.org/10.1006/niox.2000.0319
84. Bagheri H, Hajian A, Rezaei M, Shirzadmehr A (2017) Composite of Cu metal Nanoparticles-Multiwall Carbon Nanotubes-Reduced Graphene Oxide as a Novel and High Performance Platform of the Electrochemical Sensor for Simultaneous Determination of Nitrite and Nitrate. J Hazard Mater 324:762–772. https://doi.org/10.1016/j.jhazmat.2016.11.055
85. Duy LX, Peng Z, Li Y, Zhang J, Ji Y, Tour JM (2018) Laser-Induced Graphene Fibers. Carbon N Y 126:472–479. https://doi.org/10.1016/j.carbon.2017.10.036
86. Veder JP, de Marco R, Clarke G, Chester R, Nelson A, Prince K, Pretsch E, Bakker E (2008) Elimination of Undesirable Water Layers in Solid-Contact Polymeric Ion-Selective Electrodes. Anal Chem 80(17):6731–6740. https://doi.org/10.1021/ac800823f
87. Ni Z, Wang Y, Yu T, Shen Z (2008) Raman Spectroscopy and Imaging of Graphene. Nano Res 1(4):273–291. https://doi.org/10.1007/s12274-008-8036-1
88. Nguyen VT, Le HD, Nguyen VC, Ngo TTT, Le DQ, Nguyen XN, Phan NM (2013) Synthesis of Multi-Layer Graphene Films on

Copper Tape by Atmospheric Pressure Chemical Vapor Deposition Method. Adv Nat Sci: Nanosci Nanotechnol 4(3):2–7. https://doi.org/10.1088/2043-6262/4/3/035012
89. Chen Y, Long J, Zhou S, Shi D, Huang Y, Chen X, Gao J, Zhao N, Wong C (2019) UV Laser-induced Polyimide to Graphene Conversion: Modeling, Fabrication, and Application. Small Methods. https://doi.org/10.1002/smtd.201900208
90. Cardoso AR, Marques AC, Santos L, Carvalho AF, Costa FM, Martins R, Sales MGF, Fortunato E (2018) Molecularly-Imprinted Chloramphenicol Sensor with Laser-Induced Graphene Electrodes. Biosens Bioelectron 2019(124–125):167–175. https://doi.org/10.1016/j.bios.2018.10.015
91. Johnson ZT, Williams K, Chen B, Sheets R, Jared N, Li J, Smith EA, Claussen JC (2021) Electrochemical Sensing of Neonicotinoids Using Laser-Induced Graphene. ACS Sens 6(8):3063–3071. https://doi.org/10.1021/acssensors.1c01082
92. Hall LS, Hwang D, Chen B, van Belle B, Johnson ZT, Hondred JA, Gomes CL, Bartlett MD, Claussen JC (2021) All-Graphene-Based Open Fluidics for Pumpless, Small-Scale Fluid Transport via Laser-Controlled Wettability Patterning. Nanoscale Horiz 6(1):24–32. https://doi.org/10.1039/d0nh00376j
93. Torrisi F, Hasan T, Wu W, Sun Z, Lombardo A, Kulmala TS, Hsieh GW, Jung S, Bonaccorso F, Paul PJ, Chu D, Ferrari AC (2012) Inkjet-Printed Graphene Electronics. ACS Nano 6(4):2992–3006. https://doi.org/10.1021/nn2044609
94. Elgrishi N, Rountree KJ, McCarthy BD, Rountree ES, Eisenhart TT, Dempsey JL (2018) A Practical Beginner's Guide to Cyclic Voltammetry. J Chem Educ 95(2):197–206. https://doi.org/10.1021/acs.jchemed.7b00361
95. Bard AJ, Faulkner LR (2001) Electrochemical methods: fundamentals and applications. Wiley, New York
96. Aristov N, Habekost A (2015) Cyclic Voltammetry-A Versatile Electrochemical Method Investigating Electron Transfer Processes. World J Chem Education 3(5):115–119. https://doi.org/10.12691/wjce-3-5-2
97. Wang J (1994) Analytical electrochemistry. VCH, New York
98. Soares RRA, Hjort RG, Pola CC, Parate K, Reis EL, Soares NFF, McLamore ES, Claussen JC, Gomes CL (2020) Laser-Induced Graphene Electrochemical Immunosensors for Rapid and Label-Free Monitoring of Salmonella Enterica in Chicken Broth. ACS Sens. https://doi.org/10.1021/acssensors.9b02345
99. Nayak P, Kurra N, Xia C, Alshareef HN (2016) Highly Efficient Laser Scribed Graphene Electrodes for On-Chip Electrochemical Sensing Applications. Adv Electron Mater 2(10):1–11. https://doi.org/10.1002/aelm.201600185
100. Fibbioli M, Morf WE, Badertscher M, De Rooij NF, Pretsch E (2000) Potential Drifts of Solid-Contacted Ion-Selective Electrodes Due to Zero-Current Ion Fluxes through the Sensor Membrane. Electroanalysis 12(16):1286–1292. https://doi.org/10.1002/1521-4109(200011)12:16%3c1286::AID-ELAN1286%3e3.0.CO;2-Q
101. Hambly B, Guzinski M, Pendley B, Lindner E (2020) Evaluation, Pitfalls and Recommendations for the "Water Layer Test" for Solid Contact Ion-Selective Electrodes. Electroanalysis 32(4):781–791. https://doi.org/10.1002/elan.201900637
102 Han T, Kalinichev AV, Mousavi Z, Mikhelson KN, Bobacka J (2022) Anomalous Potentiometric Response of Solid-Contact Ion-Selective Electrodes with Thin-Layer Membranes. Sens Actuators B Chem 357:131416. https://doi.org/10.1016/j.snb.2022.131416
103. Paek E, Pak AJ, Hwang GS (2015) On the Influence of Polarization Effects in Predicting the Interfacial Structure and Capacitance of Graphene-like Electrodes in Ionic Liquids. Journal of Chemical Physics 142(2):024701. https://doi.org/10.1063/1.4905328
104. Ping J, Wang Y, Ying Y, Wu J (2012) Application of Electrochemically Reduced Graphene Oxide on Screen-Printed Ion-Selective Electrode. Anal Chem 84(7):3473–3479. https://doi.org/10.1021/ac203480z
105. Hu J, Stein A, Bühlmann P (2016) Rational Design of All-Solid-State Ion-Selective Electrodes and Reference Electrodes. TrAC - Trends in Analytical Chemistry. Elsevier B.V. pp 102–114. https://doi.org/10.1016/j.trac.2015.11.004
106. Schaller U, Bakker E, Spichiger UE, Pretsch E (1994) Nitrite-Selective Microelectrodes. Talanta 41(6):1001–1005
107. Sun Z, Liu X, Zhang X, Zuo M, Zou X, Niu Z, Pan H, Li J, Gao Y (2021) Single-step electrochemical sensing toward ppb-level nitrite in cured meat sensitized with functionalized Ia3d mesoporous carbon. Sens Actuators B Chem 338(March):129846. https://doi.org/10.1016/j.snb.2021.129846
108. Santos WJR, Lima PR, Tanaka AA, Tanaka SMCN, Kubota LT (2009) Determination of nitrite in food samples by anodic voltammetry using a modified electrode. Food Chem 113(4):1206–1211. https://doi.org/10.1016/j.foodchem.2008.08.009
109. Wang X, Li M, Yang S, Shan J (2020) A novel electrochemical sensor based on TiO2–Ti3C2TX/CTAB/chitosan composite for the detection of nitrite. Electrochim Acta 359:136938. https://doi.org/10.1016/j.electacta.2020.136938
110. Diouf A, el Bari N, Bouchikhi B (2019) A novel electrochemical sensor based on ion imprinted polymer and gold nanomaterials for nitrite ion analysis in exhaled breath condensate. Talanta 2020(209):120577. https://doi.org/10.1016/j.talanta.2019.120577
111. Zhang S, Dong Y, Yang Z, Yang W, Wu J, Dong C (2016) Adsorption of pharmaceuticals on chitosan-based magnetic composite particles with core-brush topology. Chem Eng J 304:325–334. https://doi.org/10.1016/j.cej.2016.06.087
112. Ficca VCA, Santoro C, Marsili E, da Silva Freitas W, Serov A, Atanassov P, Mecheri B (2022) Sensing Nitrite by Iron-Nitrogen-Carbon Oxygen Reduction Electrocatalyst. Electrochim Acta 402. https://doi.org/10.1016/j.electacta.2021.139514
113. Mani V, Dinesh B, Chen SM, Saraswathi R (2014) Direct electrochemistry of myoglobin at reduced graphene oxide-multiwalled carbon nanotubes-platinum nanoparticles nanocomposite and biosensing towards hydrogen peroxide and nitrite. Biosens Bioelectron 53:420–427. https://doi.org/10.1016/j.bios.2013.09.075
114. Cuartero M, Crespo G, Cherubini T, Pankratova N, Confalonieri F, Massa F, Tercier-Waeber ML, Abdou M, Schäfer J, Bakker E (2018) In situ detection of macronutrients and chloride in seawater by submersible electrochemical sensors. Anal Chem 90(7):4702–4710. https://doi.org/10.1021/acs.analchem.7b05299
115. Yuan X, Chen J, Ling Y, Yu S, Li S, Wu X, Zhang Z (2022) A facile and efficient nitrite electrochemical sensor based on N, O Co-doped porous graphene film. Microchem J 178. https://doi.org/10.1016/j.microc.2022.107361
116. Zhang N, Yang J, Hu C (2022) Laser-scribed graphene sensors on nail polish with tunable composition for electrochemical detection of nitrite and glucose. Sens Actuators B Chem 357(January):131394. https://doi.org/10.1016/j.snb.2022.131394
117. Nasraoui S, Al-Hamry A, Teixeira PR, Ameur S, Paterno LG, Ali MB, Kanoun O (2021) Electrochemical sensor for nitrite detection in water samples using flexible laser-induced graphene electrodes functionalized by CNT decorated by Au nanoparticles. J Electroanal Chem 880:114893. https://doi.org/10.1016/j.jelechem.2020.114893
118. Brahem A, Al-Hamry A, Gross MA, Paterno LG, Ali MB, Kanoun O (2022) Stability enhancement of laser-scribed reduced graphene oxide electrodes functionalized by iron oxide/reduced

graphene oxide nanocomposites for nitrite sensors. J Compos Sci 6(8). https://doi.org/10.3390/jcs6080221
119. CostaWRP, Rocha RG, de Faria LV, Matias TA, Ramos DLO, Dias AGC, Fernandes GL, Richter EM, Muñoz RAA (2022) Affordable equipment to fabricate laser-induced graphene electrodes for portable electrochemical sensing. Microchimica Acta 189 (5). https://doi.org/10.1007/s00604-022-05294-6
120. de Myttenaere A, Golden B, le Grand B, Rossi F (2016) Mean absolute percentage error for regression models. Neurocomputing 192:38–48. https://doi.org/10.1016/j.neucom.2015.12.114
121. Nair MS, Nair DVT, Johny AK, Venkitanarayanan K (2020) Use of food preservatives and additives in meat and their detection techniques. In: Biswas AK, Mandal PK (eds) Meat Quality Analysis - Advanced Evaluation Methods, Techniques, and Technologies, 1st edn. Academic Press, Cambridge, pp 187–213
122. Shao Y, Yao Y, Jiang C, Zhao F, Liu X, Ying Y, Ping J (2019) Two-dimensional MXene nanosheets (Types Ti3C2Tx and Ti2CTx) as new ion-to-electron transducers in solid-contact calcium ion-selective electrodes. Microchimica Acta 186 (12). https://doi.org/10.1007/s00604-019-3878-7
123. Bobacka J (1999) Potential stability of all-solid-state ion-selective electrodes using conducting polymers as ion-to-electron transducers. Anal Chem 71(21):4932–4937. https://doi.org/10.1021/ac990497z